Josephson Inductance as a Probe for Highly Ballistic Semiconductor-Superconductor Weak Links

Christian Baumgartner,[1] Lorenz Fuchs,[1] Linus Frész,[1] Simon Reinhardt,[1] Sergei Gronin,[2,3] Geoffrey C. Gardner,[2,4] Michael J. Manfra,[5,4,6,7,2] Nicola Paradiso,[1,*] and Christoph Strunk[1]

[1]*Institut für Experimentelle und Angewandte Physik, University of Regensburg, 93040 Regensburg, Germany*
[2]*Microsoft Quantum Purdue, Purdue University, West Lafayette, Indiana 47907, USA*
[3]*Birck Nanotechnology Center, Purdue University, West Lafayette, Indiana 47907, USA*
[4]*Birck Nanotechnology Center, Purdue University, West Lafayette, Indiana 47907 USA*
[5]*Department of Physics and Astronomy, Purdue University, West Lafayette, Indiana 47907, USA*
[6]*School of Materials Engineering, Purdue University, West Lafayette, Indiana 47907, USA*
[7]*School of Electrical and Computer Engineering, Purdue University, West Lafayette, Indiana 47907, USA*

(Received 21 July 2020; accepted 21 December 2020; published 21 January 2021)

We present simultaneous measurements of Josephson inductance and dc transport characteristics of ballistic Josephson junctions based upon an epitaxial Al-InAs heterostructure. The Josephson inductance at finite current bias directly reveals the current-phase relation. The proximity-induced gap, the critical current and the average value of the transparency $\bar{\tau}$ are extracted without need for phase bias, demonstrating, e.g., a near-unity value of $\bar{\tau} = 0.94$. Our method allows us to probe the devices deeply in the nondissipative regime, where ordinary transport measurements are featureless. In perpendicular magnetic field the junctions show a nearly perfect Fraunhofer pattern of the critical current, which is insensitive to the value of $\bar{\tau}$. In contrast, the signature of supercurrent interference in the inductance turns out to be extremely sensitive to $\bar{\tau}$.

DOI: 10.1103/PhysRevLett.126.037001

Epitaxial semiconductor-superconductor hybrids [1,2] have provided an important platform for new types of devices including basic elements for topological quantum computing [3]. The epitaxial growth enabled a new generation of proximity-coupled Josephson junctions (JJs) that constitutes an unique playground in modern condensed matter physics research. In such junctions, the relation $I(\varphi)$ between supercurrent I and phase difference φ between superconducting leads encodes information on the rich physics of Andreev bound states (ABS) [4–6]. Particularly exciting phenomena emerge in the presence of strong spin-orbit interaction as, e.g., for InAs-based junctions [7–9]. Topologically protected phases have been predicted [10–13] and recently demonstrated [14,15]. Moreover, simultaneous breaking of both time-reversal and parity symmetry [16] leads to an anomalous shift in the current phase relation [17–20], so that the junctions exhibit finite phase difference at zero current, and vice versa.

Current-voltage $[I(V)]$ characteristics of single junctions are simple to measure, but do not provide access to the current-phase relation (CPR). Typically, an asymmetric SQUID [21–23], or a local probe of the magnetic field [24–26] is needed to implement the phase bias. Alternatively, the phase dependence of the Josephson inductance $L(\varphi) = [(2\pi/\Phi_0) \cdot dI(\varphi)/d\varphi]^{-1}$ has been measured using a superconducting microwave resonator [27–29]. However, such resonators are usually not compatible with high magnetic fields. Another option is the interferometer-based method described in Ref. [30] which, however, does not provide access to the dc transport properties. On the other hand, it should be possible to investigate the nonlinear inductance $L(I)$ that is obtained by eliminating the unknown phase from the two equations $I(\varphi)$ and $L^{-1}(\varphi)$. This route seems so far nearly unexplored in the context of proximity-coupled JJs. In addition, measurements of individual multichannel junctions are always affected by the sample-specific defect configuration, which tends to mask the underlying generic properties of the specific semiconductor material. Hence a method is desirable, which provides an average over a large ensemble of junctions, in which the effects of individual defect configurations have negligible effect.

In this Letter we report on both the Josephson inductance and the dc transport characteristics of a linear array of about 2250 individual junctions. We show that the dependence of the Josephson inductance on current bias, magnetic field, and temperature is quantitatively understood in terms of the short ballistic junction model. From the data, we deduce an average transparency very close to one. We infer also the induced superconducting gap and the number of channels carrying the supercurrent. As opposed to the critical current, the quantum interference pattern in the inductance is very sensitive to the transparency. We find perfect consistency between the dc current and magnetic field dependence of the

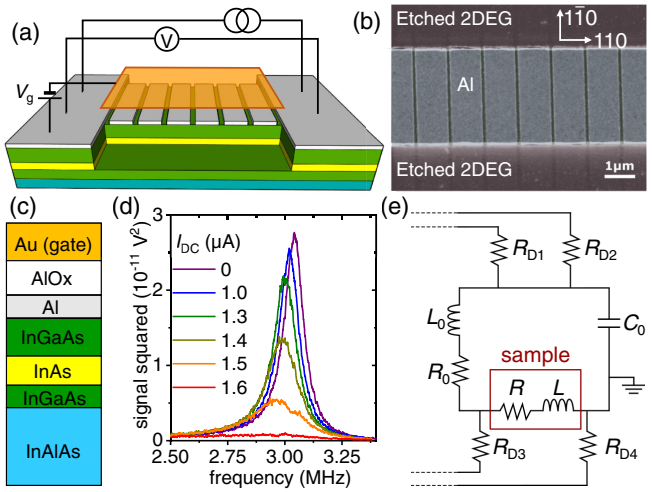

FIG. 1. (a) Schematic of the Josephson junction array. The actual array is made of 2250 Al islands. (b) Scanning electron micrograph of a portion of the array, taken prior to the deposition of the gate dielectric and of the global top gate. (c) Sequence of the topmost layers for the heterostructure under study. The Al oxide and the Au layer have been lithographically deposited after the wafer growth. (d) RLC resonance spectra for different values of the dc current through the array of Josephson junctions, measured at $T = 500$ mK. (e) Circuit scheme of the cold RLC resonator used in this work.

inductance. Our method provides a simple, versatile and robust access to the ABS physics in multichannel unconventional Josephson junctions.

Our samples are fabricated starting from a heterostructure based on a 7 nm-thick Al film epitaxially grown on top of a InGaAs/InAs quantum well [see Figs. 1(a), 1(c)], producing a shallow 2D electron gas (2DEG) [31]. The whole array is covered with a 40 nm-thick aluminum oxide layer and with a 5 nmTi/120 nm Au metal film used as a global top gate. The 2DEG underneath the epitaxial Al film is proximitized, with an induced gap $\Delta^* \approx 140$ μeV, as determined by tunnel spectroscopy [31] using a quantum point contact prepared on a separate chip from the same wafer (similar as in Ref. [32]). A JJ array of about 2250 islands is produced by standard lithographic techniques. The island width, length, and separation is 3.15, 1.0, and 0.10 μm, respectively. The Josephson inductance of such a large number of junctions in series produces a sizable total inductance, of the order of hundreds of nH. The differential inductance $L(I)$ is inferred from the resonance frequency shift [33] [see Fig. 1(d)] of a cold RLC circuit, sketched in Fig. 1(e), mounted directly on the sample holder [31]. The external inductor (capacitor) has an inductance (capacitance) $L_0 = 382$ nH ($C_0 = 4$ nF). Figure 1(d) shows typical resonance spectra for different values of the dc current bias at 500 mK. By automated fitting, we extract the center frequency and thus the array inductance L, which is reported in what follows.

The Josephson inductance is computed starting from the time derivative of the CPR $I = I_0 f(\varphi)$, where I_0 is the characteristic current scale [34], φ is the phase difference between the superconducting leads and $f(\varphi)$ a 2π-periodic dimensionless function [e.g., $f(\varphi) = \sin\varphi$ for a tunnel junction]. The ratio of Josephson voltage $V = \hbar\dot{\varphi}/2e$ and time derivative of the CPR defines the Josephson inductance

$$L(\varphi) \equiv \frac{V}{\frac{dI}{dt}} = \frac{\Phi_0}{2\pi I_0 f'(\varphi)}. \tag{1}$$

Integration of $L\dot{I} = \Phi_0\dot{\varphi}/2\pi$ provides a reconstruction of the (inverse) CPR $\varphi = \varphi(I)$:

$$\varphi(I) = \varphi(0) + \frac{2\pi}{\Phi_0}\int_0^I L(I')dI', \tag{2}$$

where $L(I)$ is the measured inductance as a function of the dc current bias. We stress that here the phase difference is controlled by the current bias, as opposed to the asymmetric SQUID method where φ is controlled by the magnetic flux in the loop.

Solid lines in Fig. 2(a) show the Josephson inductance measured as a function of current bias at different temperatures. We notice that an increase of temperature produces an increase of the zero-bias inductance $L(0)$. This is further increased by a finite current bias. In order to quantitatively describe our data, we made use of the CPR for short ballistic junctions at arbitrary temperature, which is given by [5,6,30]

$$I(\varphi) = I_0 f(\varphi) = I_0 \frac{\bar{\tau}\sin\varphi \tanh\left[\frac{\Delta^*(T)}{2k_BT}\sqrt{1-\bar{\tau}\sin^2(\frac{\varphi}{2})}\right]}{2\sqrt{1-\bar{\tau}\sin^2(\frac{\varphi}{2})}}, \tag{3}$$

where $\Delta^*(T)$ is the induced superconducting gap of the proximitized 2DEG and $\bar{\tau}$ is an average transmission coefficient [31]. Note that I_0 corresponds to the critical current only for $\bar{\tau} = 1$ and $T = 0$. We shall show that all our results are very well described by Eq. (3), even though our 2250 junctions are in the multichannel regime. The accessible part of the CPR $I(\varphi)$ corresponding to the data in Fig. 2(a) is obtained using Eq. (2) and plotted in Fig. 2(c). In order to better compare the current dependence of the curves in Fig. 2(a) with that expected from Eq. (3), we plotted them in a normalized form in Fig. 2(d). This graph shows $L(0)/L(I)$ plotted as a function of $2\pi L(0)I/\Phi_0$. This normalization allows us to express the results in a form that is sensitive only to the shape of the CPR (i.e., to $\bar{\tau}$) and not to its prefactor I_0. In Fig. 2(d) we observe that an increase of temperature produces an increase of curvature for $L(I)$. The solid and dash-dotted black lines represent the limiting cases for $\bar{\tau} \to 1$ and $\bar{\tau} \to 0$ in Eq. (3), respectively. The lowest temperature curve ($T = 100$ mK) matches with $\bar{\tau} = 0.94$. The other

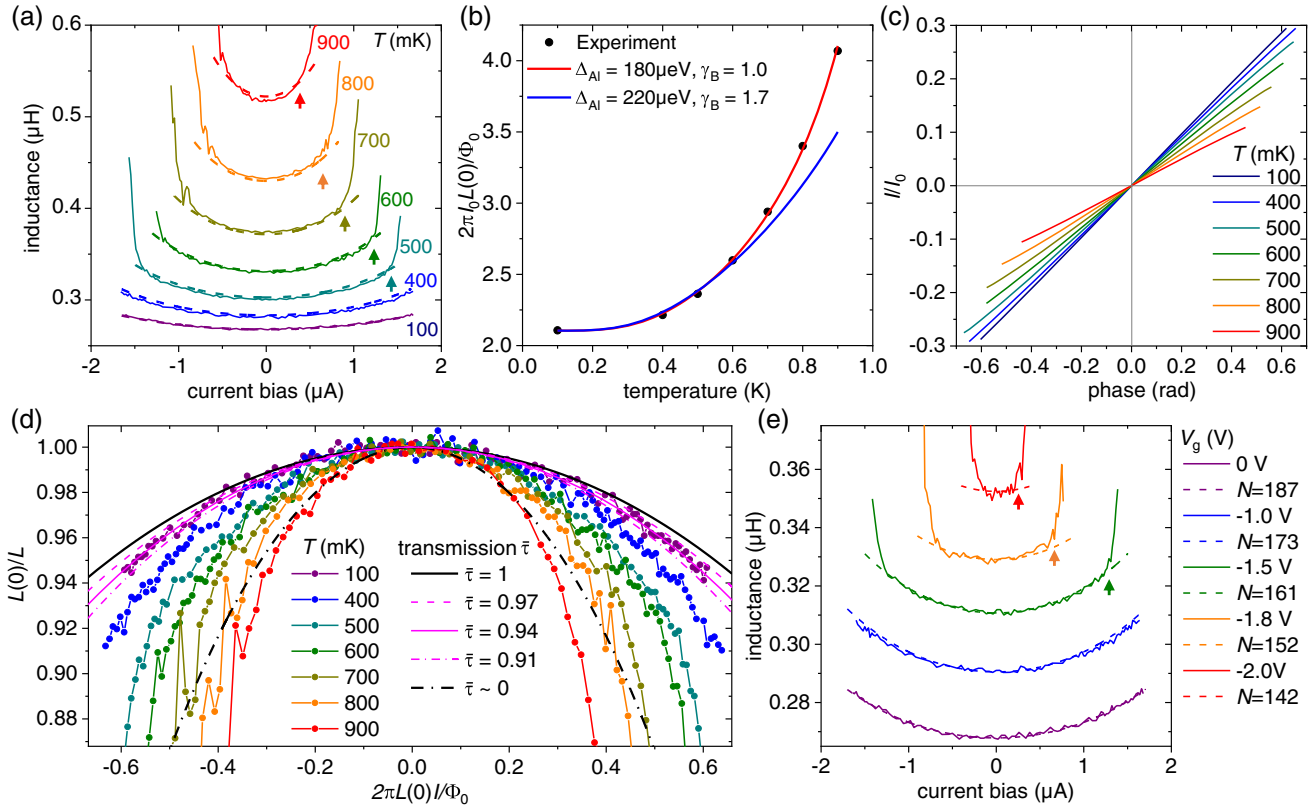

FIG. 2. (a) Josephson inductance L versus current bias I measured for different temperatures from 100 to 900 mK (solid lines). Dashed lines show L computed from Eq. (3) with parameters $I_0 = 5.882\ \mu$A, $\bar{\tau} = 0.94$, $\Delta_{\rm Al} = 180\ \mu$eV, and $\gamma_B = 1.0$ (see text). (b) Zero-bias inductance $L(0)$, normalized to $\Phi_0/(2\pi I_0)$, plotted versus temperature (symbols), together with the prediction from Eq. (3) for (red curve) $\Delta_{\rm Al} = 180\ \mu$eV, $\gamma_B = 1.0$, and (blue curve) $\Delta_{\rm Al} = 220\ \mu$eV, $\gamma_B = 1.7$. (c) CPR curves obtained by integrating data in panel (a) using Eq. (2). (d) Symbols show a normalized representation of data in panel (a) (see text). Lines show the prediction of the $T = 0$ limit of Eq. (3) for selected values of the transparency $\bar{\tau}$. (e) $L(I)$ at $T = 100$ mK plotted for different gate voltage values V_g (solid lines), together with the computed $L(I)$ from Eq. (3) (dashed lines). The number of supercurrent-carrying channels is deduced from the number N in Eq. (4) that best fits the data.

important parameter $I_0 = 5.882\ \mu$A is then obtained from the $L(0)$ value at the same temperature using Eq. (1) with $\bar{\tau} = 0.94$ in the function f. This corresponds to a critical current $I_c \equiv I_0 \max_\varphi f(\bar{\tau} = 0.94, \varphi) = 4.41\ \mu$A, which is about $0.75 I_0$.

The temperature dependence of the Josephson inductance provides the induced gap Δ^*. By fitting the measured values of $L(0)$ versus T, shown in Fig. 2(b), it is possible to extract the last two parameters of our problem, namely, the Al gap $\Delta_{\rm Al}$ and the barrier parameter γ_B between Al film and 2DEG. As discussed in Ref. [35], these two parameters determine [36–38] the temperature dependence of the induced gap Δ^* (see discussion in the Supplemental Material [31]). The fit in Fig. 2(b) (red line) provides the values $\Delta_{\rm Al} = 180\ \mu$eV and $\gamma_B = 1.0$. Alternatively, $\Delta_{\rm Al}$ can be estimated from T_c [31], leaving γ_B as the only fitting parameter. In this case the fit [blue line in Fig. 2(b)] underestimates $L(0)$ at higher temperature. In both cases, we obtain $\Delta^*(0) \approx 130\ \mu$eV, in agreement with the value found in tunneling data mentioned above.

Inserting the four parameters $\bar{\tau} = 0.94$, $I_0 = 5.882\ \mu$A, $\Delta_{\rm Al} = 180\ \mu$eV and $\gamma_B = 1.0$ just determined into Eq. (3), we obtain a consistent quantitative description of our whole set of data. We begin with Fig. 2(a). Without adjustment, the dashed lines perfectly match the curvature of $L(I)$ up to the appearance of the upwards kinks, marked with arrows. These kinks correspond to some weak junctions in the array with reduced critical current. At moderate bias their inductance is negligible compared to that of the other two thousand junctions in series. However, when the current approaches their reduced critical current value, their inductance sharply increases until it becomes dominant. At the same time, the resistance quickly increases and damps out the resonance [31]. The kinks become discontinuities at the lowest temperatures [resonance damped within one experimental point in Fig. 2(a)], indicating that there are only a few of such weaker junctions. Their reduced critical current sets the highest current at which the inductance can be measured, which is markedly less than I_0 found *at equilibrium* with inductance

measurements. This limits the accessible fraction of the CPR as shown in Fig. 2(c). We stress that, while dominating the transport at high bias, weak junctions are irrelevant at moderate bias, provided the array is long enough. The larger the number of junctions, the less important are imperfections in few of them.

Once the relevant CPR parameters have been found, it is possible to further validate our analysis by investigating the dependence of L on other parameters. Figure 2(e) shows how the measured finite-bias $L(I)$ (solid lines) depends on the gate voltage V_g. At a first glance, the curves resemble those in Fig. 2(a), i.e., L increases by increasing $|V_g|$ and $|I|$. There is, however, an important difference: in Fig. 2(e) the *curvature* is barely affected by the gate voltage, indicating that what is altered is just the prefactor I_0 and not the *shape* of the CPR. In fact, the simplest interpretation of the impact of $|V_g|$ is that it changes the number of transverse channels N that carry the supercurrent, while $\bar{\tau}$ stays constant. This alters the prefactor $I_0(V_g)$ which is given by

$$I_0(V_g) = \frac{e\Delta^*}{\hbar} N(V_g). \tag{4}$$

Using Eqs. (3) and (4), we extract $N(V_g)$ versus gate voltage from the data in Fig. 2(e) and obtain $N(0) = 187$ at $V_g = 0$. This number is very close to the value $N = [(2e^2/h)R_{sh}]^{-1} = 193$ obtained from the Sharvin resistance in the normal state, $R_{sh} = R_n = 66.9\ \Omega$. The good agreement between the two estimates of N demonstrates that I_0 is not suppressed by environment effects as often observed in $I(V)$-characteristics. The normal state resistance allows us to estimate the product I_cR_n, which can be compared with the theoretical ballistic limit $\pi\Delta^*/e$. We find that the measured $I_cR_n = 295\ \mu$V, which is 72% of the ballistic limit for $\Delta^* = 130\ \mu$eV. This fraction is close to that (69%) observed in Ref. [20] for clean junctions with a length comparable to ours.

A hallmark of the Josephson effect and an important indicator for junction homogeneity is the modulation of the critical current $I_c(B_\perp)$ by quantum interference in a perpendicular magnetic field $B_\perp$. Figure 3(a) shows the JJ array resistance measured in dc as a function of $B_\perp$ and I at $T = 100$ mK. The resistance is obtained by numerical differentiation of IV characteristics. The diffraction pattern $I_c(B_\perp)$ is visible as the boundary between near-zero and finite resistance regions. It matches the Fraunhofer pattern well known from tunneling junctions: $I_c(B_\perp) = I_c(0)|\sin(\pi\Phi/\Phi_0)/(\pi\Phi/\Phi_0)|$. This is not by accident: the normalized diffraction pattern $I_c(B_\perp)/I_c(0)$ calculated from Eq. (3) by integrating the current density over the width of the junctions turns out to be independent of $\bar{\tau}$ [31].

The period of the diffraction pattern is determined by the flux $\Phi = awB_\perp$ within the effective junction area, where w and a are width and effective length, respectively. From the lobe periodicity in Fig. 3(a) we find $a = 960$ nm. This is close to the lattice period $a_0 = 1.1\ \mu$m of the array [39]. At $B_\perp = 0$, most JJs switch to normal resistance at current bias of $2.4\ \mu$A, which is considerably less than the critical current $I_c = 4.41\ \mu$A defined above. The reason for the discrepancy is once again the presence of weaker junctions. Once they switch to normal resistance, their dissipation heats the remaining junctions, leading to a runaway process that rapidly brings the whole array into the normal state.

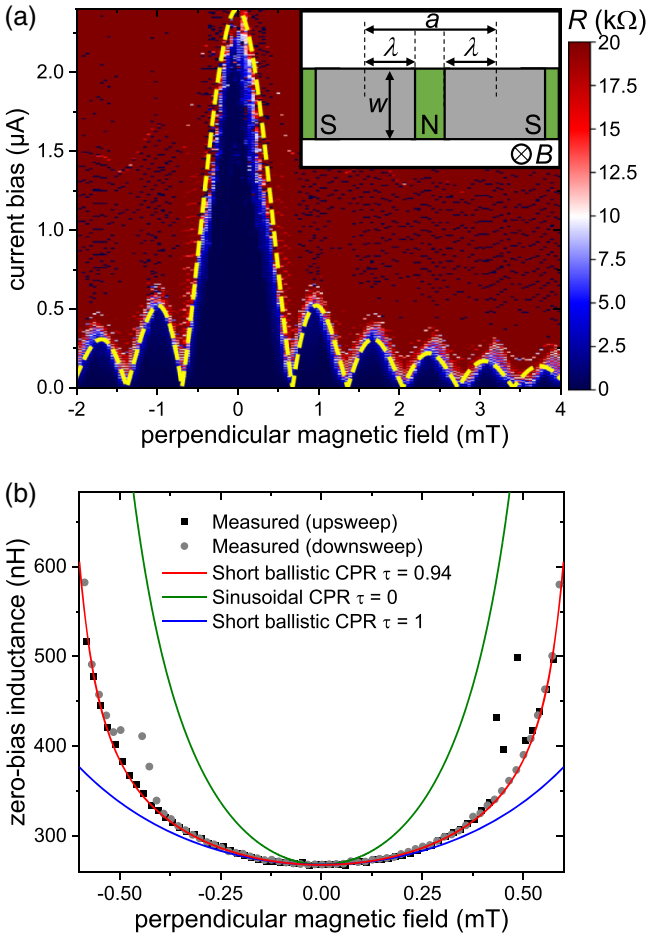

FIG. 3. (a) Color plot of the differential resistance plotted as a function of perpendicular magnetic field $B_\perp$ and current bias. The dashed yellow line shows the expected critical current $I_c(B_\perp)$ for a rectangular junction with effective length $a = 960$ nm and width $w = 3.15\ \mu$m, see inset. (b) Zero-bias Josephson inductance L as a function of $B_\perp$ for the central lobe in the diffraction pattern (symbols) together with the curves deduced from Eq. (3) for $\bar{\tau} = 0.94$ (red), $\bar{\tau} \to 1$ (blue), and $\bar{\tau} \to 0$ (green). For the latter curve, the parameter I_0 has been rescaled by a factor 2.06 to match the measured zero-field inductance [31].

In order to substantiate our evaluation of the average transparency $\bar{\tau}$ against yet another observable, we turn now to the dependence of the zero bias Josephson inductance on $B_\perp$. In contrast to the critical current, the diffraction pattern in L turns out to be very sensitive to $\bar{\tau}$. This is demonstrated in Fig. 3(b), displaying the measured inductance $L(B_\perp)$ for the central lobe (symbols) together with the expectation for

$L(B_\perp)$ (red solid line) using the CPR in Eq. (3). Without further adjustment of the previously determined parameters I_0, $\bar{\tau}$, and a, we find an excellent agreement that corroborates our analysis. The green and blue curve show instead the limiting cases of perfect opacity ($\bar{\tau} \to 0$, sinusoidal CPR, green curve) and perfect transparency ($\bar{\tau} \to 1$, blue curve) case, respectively. For the latter cases, the value of I_0 has been rescaled to obtain the measured value of zero-field inductance. It is clear that, even then, CPRs with values of $\bar{\tau} \neq 0.94$ cannot reproduce the experimental data. Instead, Eq. (3) with $\bar{\tau} = 0.94$ correctly describes not only the equilibrium $L(B_\perp)$, but also the curves for finite current bias [31].

In conclusion, we have shown that the Josephson inductance is a sensitive and versatile probe of the Andreev spectrum in short ballistic SNS junctions. The temperature, bias, gate voltage, and perpendicular field dependence of the Josephson inductance can be quantitatively described in terms of a short ballistic weak link with nearly perfect transmission. Inductance measurements enable the direct determination of the induced gap and of the junction transparency. Our experimental scheme can be easily combined with standard dc setups and allows for a simultaneous measurement of dc transport properties.

We thank Asbjørn Drachmann, Charles M. Marcus, and Marco Aprili for stimulating discussions. Work at UR was funded by the Deutsche Forschungsgemeinschaft (DFG, German Research Foundation)—Project-ID 314695032—SFB 1277 (Subproject B08). Work completed at Purdue University is supported by Microsoft Quantum.

*nicola.paradiso@physik.uni-regensburg.de

[1] P. Krogstrup, N. L. B. Ziino, W. Chang, S. M. Albrecht, M. H. Madsen, E. Johnson, J. Nygård, C. M. Marcus, and T. S. Jespersen, Nat. Mater. **14**, 400 (2015).
[2] W. Chang, S. M. Albrecht, T. S. Jespersen, F. Kuemmeth, P. Krogstrup, J. Nygård, and C. M. Marcus, Nat. Nanotechnol. **10**, 232 (2015).
[3] J. Shabani, M. Kjaergaard, H. J. Suominen, Y. Kim, F. Nichele, K. Pakrouski, T. Stankevic, R. M. Lutchyn, P. Krogstrup, R. Feidenhans'l, S. Kraemer, C. Nayak, M. Troyer, C. M. Marcus, and C. J. Palmstrøm, Phys. Rev. B **93**, 155402 (2016).
[4] A. Furusaki and M. Tsukada, Solid State Commun. **78**, 299 (1991).
[5] C. W. J. Beenakker and H. van Houten, Phys. Rev. Lett. **66**, 3056 (1991).
[6] M. L. Della Rocca, M. Chauvin, B. Huard, H. Pothier, D. Esteve, and C. Urbina, Phys. Rev. Lett. **99**, 127005 (2007).
[7] F. K. de Vries, T. Timmerman, V. P. Ostroukh, J. van Veen, A. J. A. Beukman, F. Qu, M. Wimmer, B.-M. Nguyen, A. A. Kiselev, W. Yi, M. Sokolich, M. J. Manfra, C. M. Marcus, and L. P. Kouwenhoven, Phys. Rev. Lett. **120**, 047702 (2018).
[8] C. T. Ke, C. M. Moehle, F. K. de Vries, C. Thomas, S. Metti, C. R. Guinn, R. Kallaher, M. Lodari, G. Scappucci, T. Wang, R. E. Diaz, G. C. Gardner, M. J. Manfra, and S. Goswami, Nat. Commun. **10**, 3764 (2019).
[9] W. Mayer, J. Yuan, K. S. Wickramasinghe, T. Nguyen, M. C. Dartiailh, and J. Shabani, Appl. Phys. Lett. **114**, 103104 (2019).
[10] J. Alicea, Rep. Prog. Phys. **75**, 076501 (2012).
[11] M. Hell, M. Leijnse, and K. Flensberg, Phys. Rev. Lett. **118**, 107701 (2017).
[12] F. Pientka, A. Keselman, E. Berg, A. Yacoby, A. Stern, and B. I. Halperin, Phys. Rev. X **7**, 021032 (2017).
[13] B. Scharf, F. Pientka, H. Ren, A. Yacoby, and E. M. Hankiewicz, Phys. Rev. B **99**, 214503 (2019).
[14] H. Ren, F. Pientka, S. Hart, A. T. Pierce, M. Kosowsky, L. Lunczer, R. Schlereth, B. Scharf, E. M. Hankiewicz, L. W. Molenkamp, B. I. Halperin, and A. Yacoby, Nature (London) **569**, 93 (2019).
[15] A. Fornieri, A. M. Whiticar, F. Setiawan, E. Portolés, A. C. C. Drachmann, A. Keselman, S. Gronin, C. Thomas, T. Wang, R. Kallaher, G. C. Gardner, E. Berg, M. J. Manfra, A. Stern, C. M. Marcus, and F. Nichele, Nature (London) **569**, 89 (2019).
[16] A. Rasmussen, J. Danon, H. Suominen, F. Nichele, M. Kjaergaard, and K. Flensberg, Phys. Rev. B **93**, 155406 (2016).
[17] A. A. Reynoso, G. Usaj, C. A. Balseiro, D. Feinberg, and M. Avignon, Phys. Rev. Lett. **101**, 107001 (2008).
[18] T. Yokoyama, M. Eto, and Y. V. Nazarov, Phys. Rev. B **89**, 195407 (2014).
[19] D. B. Szombati, S. Nadj-Perge, D. Car, S. R. Plissard, E. P. A. M. Bakkers, and L. P. Kouwenhoven, Nat. Phys. **12**, 568 (2016).
[20] W. Mayer, M. C. Dartiailh, J. Yuan, K. S. Wickramasinghe, E. Rossi, and J. Shabani, Nat. Commun. **11**, 212 (2020).
[21] R. Delagrange, D. J. Luitz, R. Weil, A. Kasumov, V. Meden, H. Bouchiat, and R. Deblock, Phys. Rev. B **91**, 241401(R) (2015).
[22] A. Murani, A. Kasumov, S. Sengupta, Y. A. Kasumov, V. T. Volkov, I. I. Khodos, F. Brisset, R. Delagrange, A. Chepelianskii, R. Deblock, H. Bouchiat, and S. Guéron, Nat. Commun. **8**, 15941 (2017).
[23] C. Li, J. C. de Boer, B. de Ronde, S. V. Ramankutty, E. van Heumen, Y. Huang, A. de Visser, A. A. Golubov, M. S. Golden, and A. Brinkman, Nat. Mater. **17**, 875 (2018).
[24] M. Fuechsle, J. Bentner, D. A. Ryndyk, M. Reinwald, W. Wegscheider, and C. Strunk, Phys. Rev. Lett. **102**, 127001 (2009).
[25] E. M. Spanton, M. Deng, S. Vaitiekėnas, P. Krogstrup, J. Nygård, C. M. Marcus, and K. A. Moler, Nat. Phys. **13**, 1177 (2017).
[26] S. Hart, Z. Cui, G. Ménard, M. Deng, A. E. Antipov, R. M. Lutchyn, P. Krogstrup, C. M. Marcus, and K. A. Moler, Phys. Rev. B **100**, 064523 (2019).
[27] B. Dassonneville, M. Ferrier, S. Guéron, and H. Bouchiat, Phys. Rev. Lett. **110**, 217001 (2013).
[28] A. Murani, B. Dassonneville, A. Kasumov, J. Basset, M. Ferrier, R. Deblock, S. Guéron, and H. Bouchiat, Phys. Rev. Lett. **122**, 076802 (2019).

[29] L. Tosi, C. Metzger, M. F. Goffman, C. Urbina, H. Pothier, S. Park, A. L. Yeyati, J. Nygård, and P. Krogstrup, Phys. Rev. X **9**, 011010 (2019).
[30] A. A. Golubov, M. Y. Kupriyanov, and E. Il'ichev, Rev. Mod. Phys. **76**, 411 (2004).
[31] See Supplemental Material at http://link.aps.org/supplemental/10.1103/PhysRevLett.126.037001 for further information.
[32] M. Kjaergaard, F. Nichele, H. J. Suominen, M. P. Nowak, M. Wimmer, A. R. Akhmerov, J. A. Folk, K. Flensberg, J. Shabani, C. J. Palmstrøm, and C. M. Marcus, Nat. Commun. **7**, 12841 (2016).
[33] R. Meservey and P. M. Tedrow, J. Appl. Phys. **40**, 2028 (1969).
[34] If max $|f(\varphi)| = 1$, then I_0 is the critical current of the junction.
[35] M. Kjaergaard, H. J. Suominen, M. P. Nowak, A. R. Akhmerov, J. Shabani, C. J. Palmstrøm, F. Nichele, and C. M. Marcus, Phys. Rev. Applied **7**, 034029 (2017).
[36] A. Chrestin, T. Matsuyama, and U. Merkt, Phys. Rev. B **55**, 8457 (1997).
[37] B. A. Aminov, A. A. Golubov, and M. Y. Kupriyanov, Phys. Rev. B **53**, 365 (1996).
[38] T. Schäpers, *Superconductor/Semiconductor Junctions*, International Series in Pure and Applied Physics Vol. 174 (Springer, Berlin, 2001).
[39] The length a is usually estimated as the spacing between the Al islands plus twice the effective magnetic penetration depth. In large films of thickness d the field penetrates up to a length [40,41] $\lambda_\perp = \lambda_L^2/d$, where λ_L is the London penetration depth. In our case $\lambda_L = 220$ nm, as obtained from independent measurements of the kinetic inductance of the same heterostructure, which is also in reasonable agreement with the estimate from the normal state resistance. Since $\lambda_\perp \simeq 8\ \mu$m is much larger than the Al island size, the field penetrates them almost completely. Thus, the value of the effective junction length a is expected to be close to the junction periodicity, as verified by the Fraunhofer pattern measurement and confirmed by the good agreement between red curve and experimental points in Fig. 3(b).
[40] J. Pearl, Appl. Phys. Lett. **5**, 65 (1964).
[41] M. Tinkham, *Introduction to Superconductivity*, International Series in Pure and Applied Physics (McGraw-Hill, New York, 1975).